High resolution in-vivo DT-CMR using an interleaved variable density spiral STEAM sequence

Margarita Gorodezky[1,2], Pedro F Ferreira[1,2], Sonia Nielles-Vallespin[1], Peter D Gatehouse[1,2], Dudley J Pennell[1,2], Andrew D Scott[1,2]*, David N Firmin[1,2]*

* Andrew D Scott and David N Firmin contributed equally to this work

1. Cardiovascular Magnetic Resonance Unit London, Royal Brompton Hospital, Sydney Street, London, SW3 6NP, UK.
2. National Heart and Lung Institute, Imperial College, Sydney Street, London, SW3 6NP, UK.

Corresponding author:

Andrew Scott, Cardiovascular Magnetic Resonance Unit London, Royal Brompton Hospital, Sydney Street, London, SW3 6NP, UK.

Email: a.scott@rbht.nhs.uk

Phone: 0044 207 352 8121 Ext. 2937.

Key words: DTI, interleaved variable-density spiral readout, STEAM, in vivo, cardiac

Running head: High resolution in-vivo DT-CMR using an interleaved variable density spiral STEAM sequence

Word count: 5,262

This work was supported by Heart Research UK grant RG2648.

Abstract

Purpose: Diffusion tensor cardiovascular magnetic resonance (DT-CMR) has a limited spatial resolution. The purpose of this study was to demonstrate high-resolution DT-CMR using a segmented variable density spiral sequence with correction for motion, off-resonance and T2* related blurring.

Methods: A single-shot STEAM EPI DT-CMR sequence at 2.8x2.8x8mm^3 and 1.8x1.8x8mm^3 was compared to a single shot spiral at 2.8x2.8x8mm^3 and an interleaved spiral sequence at 1.8x1.8x8mm^3 resolution in 10 healthy volunteers at peak-systole and diastasis. Motion-induced phase was corrected using the densely sampled central k-space data of the spirals. STEAM field maps and T2* measures were obtained using a pair of stimulated echoes each with a double spiral readout, the first used to correct the motion-induced phase of the second.

Results: The high resolution spiral sequence produced similar DT-CMR results and quality measures to the standard resolution sequence in both cardiac phases. Residual differences in fractional anisotropy and helix angle gradient between the resolutions could be due to spatial resolution and/or signal to noise ratio. The data quality increased after both motion-induced phase correction and off-resonance correction and sharpness increased after T2* correction. The high resolution EPI sequence failed to provide sufficient data quality for DT-CMR reconstruction.

Conclusion: In this study an in-vivo DT-CMR acquisition at 1.8x1.8mm^2 in-plane resolution was demonstrated using a segmented spiral STEAM sequence. The motion-induced phase and off-resonance corrections are essential for high resolution spiral DT-CMR. Segmented variable density spiral STEAM was found to be the optimal method for acquiring high resolution DT-CMR data.

Introduction:

Diffusion tensor cardiovascular magnetic resonance (DT-CMR) is a unique non-invasive technique that provides insight into myocardial microstructure (1–4) and has potential impact in diagnosis or assessing treatment efficacy for diseases such as cardiomyopathy (3,5–7) and myocardial infarction (8–10). However, the spatial resolution of this technique is limited, meaning that it cannot be applied usefully in patient cohorts with a thinned myocardium, such as chronic myocardial infarction or in diseases of the right ventricle.

DT-CMR data is typically acquired using a single shot echo-planar-imaging (EPI) readout (2,11) and the spatial resolution is limited by the reduction in signal to noise ratio and increasing prevalence of artefacts as the readout duration increases. Increased spatial resolution in cardiovascular magnetic resonance (CMR) (12) and diffusion tensor (DT) neuroimaging acquisitions is often achieved via segmented acquisitions, where the required k-space data is covered in several distinct readout blocks, echo trains or trajectories (13–15). However, while there have been demonstrations of diffusion weighted CMR using segmented acquisitions (16), to our knowledge, segmented readouts have not been used for in-vivo DT-CMR.

Segmenting diffusion tensor acquisitions is complicated by bulk motion during diffusion encoding, which results in image phase shifts that can be different between segments and therefore lead to signal drop-out when the segments are combined in complex space. Phase navigators, additional echoes used to estimate the motion-induced phase, have been used to correct for the phase differences in neurological diffusion imaging (17–19). However, as bulk motion is predominantly low spatial frequency and is therefore encoded near the centre of the k-space, techniques that acquire the centre of k-space in each segment can dispense with the additional echo. These so-called self-

navigated techniques include periodically rotated overlapping parallel lines with enhanced reconstruction (PROPELLER) (20) and self-navigated interleaved spiral (SNAILS) (21).

In recent work, we took advantage of the three RF pulses used in the frequently employed stimulated echo acquisition mode (STEAM) DT-CMR sequence (2,11,22) to selectively image a small field of view around the left ventricle using a single shot spiral trajectory (23). The considerably shorter echo time available with the centre out spiral trajectory results in substantially increased SNR relative to the equivalent single shot EPI STEAM sequence.

In this work we develop our spiral STEAM DT-CMR sequence further by using a segmented variable density spiral trajectory to increase spatial resolution. We aim to demonstrate high-resolution segmented spiral DT-CMR in both peak systole and diastasis and compare this method against existing single shot EPI methods. We also introduce novel approaches to calculating B0 field maps for off-resonance correction of the spirals and a method for correcting for T2* decay during the spiral readout.

Methods

An interleaved spiral STEAM DT-CMR sequence was implemented using variable density spiral trajectories and a novel STEAM compatible field mapping technique. The motion-induced phase is estimated from the variable density spirals and used to correct inter-interleaf phase differences. The B0 field maps are used to correct for off-resonance effects. Finally, left ventricular T2* was estimated from the data and used to correct high-frequency filtering caused by T2* decay during the spiral.

Sequence design

STEAM DT-CMR minimises the effects of motion during the diffusion encoding gradients by using two monopolar diffusion encoding gradients applied at the same time in two successive cardiac cycles.
Four different STEAM sequences were used to acquire the data in this study (Figure 1). Standard resolution data was acquired with a widely used EPI sequence (Figure 1a) and a single shot spiral sequence (Figure 1b), both described in Gorodezky et al. (23). High resolution data was acquired with the same single shot EPI sequence with a longer echo train (Figure 1c) and a segmented variable density spiral STEAM sequence with two variable density spiral interleaves acquired over four consecutive cardiac cycles (Figure 1d). For all sequences a chemical-shift selective fat saturation pulse is applied before the first 90˚ pulse of each stimulated echo. The field of view (FOV) was reduced (24,25) in the phase encode direction for the EPI sequences and in both in-plane directions for the spiral sequences.

To correct for the off-resonance artefacts in the spiral data, a map of B0 inhomogeneity is needed. A field map was collected at the beginning of each breath-hold using two stimulated echoes acquired over four cardiac cycles. Typically, these field maps are calculated from (at least) two images at different echo times. Due to the nature of the STEAM sequence, the off-resonance related dephasing is refocused at TE (see Figure 1, much like in a spin-echo). However, by shifting the start of the spiral readout relative to the stimulated echo, it is possible to measure an off-resonance related phase change in the data.

A further complication arises as the spoiler gradients used to spoil non-stimulated echo pathways mean that the stimulated echoes used to generate the field maps, also contain motion-induced phase. This motion-induced phase is indistinguishable from the field inhomogeneity related phase changes which we aim to map. In order to account for this, each stimulated echo acquired for the field map calculation uses two readouts (Figure 2). The first readouts (red in Figure 2) are used to estimate the motion-induced phase of that echo. This phase is then applied (as described below) to correct the subsequent readouts (green in Figure 2). Data from these two corrected images are then used to calculate a pixel-wise field map via $\Delta f = \frac{(\varphi_1 - \varphi_2)}{2\,\pi\,\Delta\,TE_{FM}}$, where φ_1 and φ_2 are the phases in image 1 and 2 respectively and ΔTE_{FM} is the difference in the delay after the echo (TE_{FM}) between the two readouts.

Motion-induced phase correction

As described above, combining two interleaves with different bulk motion-induced phases in complex space can lead to signal loss (shown in Figure 3). In order to correct for this effect in the segmented spiral imaging data, the phase of the second interleaf was corrected to match the first interleaf (20,26). Assuming that the motion-induced phase is contained within the low-resolution fully-sampled central k-space data, we acquired variable density spiral trajectories with a higher sampling density, and therefore larger FOV near the centre of k-space (27). A Gaussian window (FWHM was 60% of k-space diameter) was applied to the gridded k-space data for both interleaves, leaving only the densely sampled central k-space data. The phase difference between the interleaves was calculated in image space and applied to the full-resolution version of the second interleaf. Figure 3 shows the restored signal in the image when the corrected interleaves are combined.

Off-resonance correction

A frequency segmented reconstruction (FSR) off-resonance correction was implemented. The spiral images were reconstructed with at least $4(f_{max}\text{-}f_{min})T_{acq}$ off-resonance offsets (28), where f_{max}/f_{min} are the maximal/minimal frequency offsets automatically detected from the magnitude-thresholded region of the field map around the LV and T_{acq} is the spiral readout duration. Each reconstructed pixel was calculated as a linear interpolation of the two reconstructions spanning the off-resonance measured in the field map.

T2* blurring correction

In order to compensate for T2* related loss of high spatial frequencies caused by T2* decay during the spiral readouts used for DT-CMR data acquisition, we estimated the mean myocardial T2* in each breath-hold. T2* was calculated from the data acquired for the field maps, on the assumption of uniform myocardial T2* and that all received signal originated in the myocardium. Spirals TS1 and TS2 in Figure 2 were used to calculate the signal decay as $T_{2\,\mathrm{decay}}^{*} = \frac{\Delta \mathrm{TE}_{T2^*}}{\log\left(\sum_{i=1}^{1000} \mathrm{FM1(i)} / \sum_{i=1}^{1000} \mathrm{FM2(i)}\right)}$, where $\sum_{i=1}^{1000} \mathrm{FM}j(\mathrm{i})$ is the sum of the magnitudes of the first 1000 k-space points of the jth spiral (j=1 for TS1 and j=2 for TS2). The spiral trajectories were corrected before the gridding via $k(t) = k(t) * e^{t/T_{2decay}^{*}}$, where k(t) are the acquired k-space data and t is the acquisition time of each point.

Study design

Data acquisition

10 healthy volunteers (3/7 female/male) mean age 30 years (range 20-53) were imaged on a 3T Skyra (Siemens Healthcare, Erlangen Germany) with an 18 element anterior and 8-12 elements of a posterior spine coil.

Data were acquired in systole using the single-shot spiral and single-shot EPI STEAM DT-CMR sequence at 2.8x2.8x8mm^3 spatial resolution and using the segmented spiral and single-shot EPI STEAM DT-CMR technique at 1.8x1.8x8mm^3 spatial resolution. Due to time limitations, in diastole only single-shot spiral data with a spatial resolution of 2.8x2.8x8mm^3 and segmented spiral data at 1.8x1.8x8mm^3 spatial resolution were acquired.

For all sequences, the target diffusion weighting was b_{ref}/b_{main}=150/600 s/mm^2 (29) and six diffusion encoding directions were used. To account for the heart rate influence on the b values, the prescribed b_{main} was adjusted depending on the subject's heart rate as follows: b_{main}=500, 600, 650, 700 s/mm^2 for the heart rates <50, 50-65, 65-70, >70 bpm respectively. b_{ref} was maintained at 150s/mm^2 as the corresponding adjustments were considered small. The stimulated echo FOV for both spiral sequences was reduced to 96x96mm^2 using a time-reversed pair of asymmetric RF pulses with in-plane slice-select gradients (23). For the high resolution acquisition the variable density spirals were designed using the software available at (30). For this type of spiral, the FOV varies with the position along the spiral. At the centre of k-space it was 95x95mm^2 (i.e. 99% sampled) and at the end of the spiral it was 55x55mm^2, which after combining the interleaves results in a readout FOV of 190-110x190-110mm^2. The spiral duration used for the field map acquisition was 5ms, resulting in an in-plane spatial resolution of 6x6mm^2 with a slice thickness of 8mm. To remain flexible to the range of off-resonance frequencies included in the reconstructed field map, images were acquired with ΔTE_{FM}=0,0,2 and 3ms after the stimulated echo in the first four stimulated echoes of each breath-hold. Further acquisition parameters can be found in Table 1.

Each average of the EPI sequence consisted of two cardiac cycles for each of the following: EPI phase correction lines, parallel imaging reference data, a "b_0" image, that was not used in reconstructions, and diffusion weighted images in the 6 directions, resulting in 18 cardiac cycles per breath-hold. The spiral acquisition is schematically demonstrated in Figure 2 and consisted of 20 cardiac cycles: 8 cardiac cycles (4 stimulated echoes) were used for the field map acquisitions and 12 cardiac cycles were used for the diffusion weighted images (6 stimulated echoes). During the single shot spiral acquisitions 6 diffusion directions were acquired per breath-hold. For the interleaved sequence 3 diffusion directions with both interleaves were acquired per breath-hold leading to the 6 diffusion encoding directions being split over two breath-holds.

Data processing

STEAM EPI DT-CMR data was reconstructed online using the standard product reconstruction. The spiral sequences were reconstructed offline in MATLAB (MathWorks, Natick, MA, USA) using the GNUFFT (31) algorithm with voronoi-based density compensation (32). In order to reduce noise floor effects, the spiral data from each of the receiver coils was combined using the maximized SNR technique (33). The coil sensitivity maps were calculated from the first four spiral readouts acquired for the field map calculation in each breath-hold.

Multiple reconstruction of the high resolution interleaved spiral systolic data were performed to demonstrate the effect of each correction: 1. no corrections; 2. a motion-induced phase correction; 3. motion-induced phase and FSR off-resonance corrections; 4. motion-induced phase correction, FSR

and T2* corrections. The spiral diastolic data was reconstructed only once with all of the relevant corrections applied. Based on initial testing ΔTE_{FM}=0 and 2ms were used for the field map calculations and ΔTE_{T2*} for the T2* correction was ΔTE_{T2*}=9.2ms (Figure 2). The high resolution spiral diastolic and both standard resolution spiral data sets were reconstructed only once with all of the relevant corrections applied.

The high resolution spiral data was reconstructed twice: first to match the number of averages acquired with the single-shot data (number matched, NM); and then to match the acquisition time (time matched, TM). For the NM reconstructions b_{ref}/b_{main}=1/8 averages for all 6 diffusion directions were used. For the TM reconstructions 4 averages of all 6 diffusion directions were used for b_{main} and one average of 3 diffusion directions were used for b_{ref}.
The tensor calculation was performed pixel-wise using in-house MATLAB software (5) using a linear least-square algorithm. The b-values were corrected for the actual duration of the cardiac cycle and were not averaged before being included into the tensor calculation. The DT-CMR analysis was performed on the left ventricle (LV) and FA, MD, eigenvalues (EV), transmural helix angle (HA) gradient (HAG) in °/% myocardial thickness, transverse angle (TA) and median absolute secondary eigenvector angulation (E2A) (5,29,34) were calculated excluding the papillary muscles and the septo-marginal trabeculations of the right ventricle. For the HAG comparison, only HA profiles with an $R^2 \geq 0.3$ and a negative slope were considered (23), based on an assumption of a transmural linear variation in HA. Single image SNR maps were calculated for the b=600s/mm^2 data over the LV using the multiple repetitions method, as described in (11,35) and averaged over the 6 diffusion directions. Due to the small number of averages, SNR was not calculated for the TM data. A comparison of the endocardial sharpness was performed in the septal wall, where there are fewest papillary muscles and trabeculations and little off-resonance artefact. Line profiles were drawn from the LV centroid to the epicardium and fitted with the sigmoid function $f(x, a_0, a_1, a_2, s) = \frac{a_1}{1+10^{s(a_0-x)}} + a_2$ (36) with x increasing positively along the profile. The parameters a_i are used to quantify the location (a_0) and amplitude of upper (a1+a2) and lower plateau (a_2) of the profile and s the growth rate or sharpness of the line-profiles. The sharpness was calculated as the median of the values of s in the septum for each subject. The quality of the acquisitions was assessed via the percentage of negative EV (%negEV) in the LV, the linearity of the HAG fit using R^2 (23,37), the fraction of the accepted R^2 (fraR^2) and the standard deviation of the TA (stdTA) (37) which is assumed to be small in healthy myocardium. In a previous study the standard resolution spiral sequence was compared to a standard resolution EPI sequence (23). In this work comparisons are performed between the standard and high-resolution data from each sequence. Statistical analysis was performed with a Wilcoxon signed rank test and $p<0.05$ was considered to be significant.

Results

The acquisition time including planning was 60 to 90 minutes. The mean heart rate corrected b-value was b_{main}=606 (range 525-688) s/mm^2. The median and interquartile range of T2* over all subjects and spiral sequences estimated from the spiral data was T2*=34±7 ms.

Comparison of the standard to high resolution sequences

Comparison of the number matched reconstruction

For all spiral sequences described in this section, the NM reconstruction with all corrections was used. DT-CMR results are compared between the standard and high resolution acquisitions for the same readout type and cardiac phase. Figure 4 and Figure 5 show DT-CMR, SNR and field maps for a typical volunteer for all the sequences for the standard and high resolution respectively. While the high resolution spiral data produced DT-CMR maps that were visually similar to the standard resolution data, the high resolution EPI data appeared noisy, with a normal pattern of HA in the septum but poor results in the rest of the left ventricle. Figure 6 shows a subject-wise comparison of FA, MD, HAG and E2A over the left ventricle for all four sequences at the two cardiac phases. The median and interquartile ranges for the plotted values are summarised in Supporting Information Table S1. All DT-CMR parameters for spiral data apart from FA and diastolic HAG showed no significant differences between the standard and high resolutions with $P>0.10$. Comparing the high to the standard resolution data, FA significantly increased ($P<0.03$) by 21% with EPI in systole, 5% and 4% for systolic and diastolic NM spiral data respectively. The magnitude of HAG significantly increases by 60% in diastasis for the high resolution spiral data. The EPI sequence showed significant differences between standard and high resolution data for all DT-CMR parameters apart from HAG (P=0.32).

The quality measurements %negEv, R^2, $fraR^2$ and SNR are shown in Figure 7. There were no significant differences ($P>0.15$) between the systolic high and standard resolution spiral acquisitions in any of these quality measures. There was no significant difference in %negEV when increasing the spiral spatial resolution in diastole, but R^2 and $fraR^2$ were both significantly higher at the higher spatial resolution. At the higher resolution the SNR significantly ($P=0.002$) decreased by 63% for systolic EPI, 29% and 36% for spiral systole and diastasis respectively. All of the quality measures changed significantly when going from standard to high resolution EPI acquisitions ($P=0.002$). Most notably the mean %negEV increased from 0.5% to 14.7% when increasing the EPI resolution, while mean %negEV was between 0.3% and 2.9% for the spiral sequences. The sharpness increased significantly when going from the standard to high resolution spiral sequence ($P<0.03$) as shown in Supporting Information Figure S1.

Comparison of the time matched reconstruction

The standard resolution spiral data described above was also compared to the TM reconstructions of the high resolution data. Supporting Information Figure S2 shows the FA, MD, HAG, E2A, %negEV and R^2 for the spiral data for the standard and high resolution NM and TM reconstructions for both cardiac phases. E2A and diastolic MD showed no significant differences between the TM high resolution and standard resolution spiral data. HAG significantly decreased (helix angle gradient becomes steeper) for the TM data compared to the standard resolution by 24% and 64% for systole and diastole respectively and FA significantly increases by 9% and 6% for systole and diastasis respectively while systolic MD significantly increased by 9%. The lower number of averages generally resulted in a lower data quality. Nevertheless, R^2 and %negEV from the TM reconstruction showed no significant changes ($P=0.38$) compared to the standard resolution case in diastasis. Systolic R^2 significantly increased from 0.84 using TM high resolution to 0.94 at standard resolution and %negEV significantly increased from 0.5% to 1.1%.

Assessment of the optimal spiral reconstruction method

Phase and off-resonance corrections

The correction methods were compared for the systolic data at both resolutions. A set of images for the 6 diffusions encoding direction is shown in Supporting Information Figure S3, showing the effects of adding each correction into the reconstruction. Figure 8 demonstrates the effects of the correction methods for a typical diffusion weighted image at 1.8x1.8mm^2 in-plane resolution. Much of the signal loss observed without any correction is restored by the motion-induced phase correction and the focussing effects of the off-resonance correction. As a consequence, signal in the lateral wall, which is most affected by off-resonance artefacts, is restored.

Supporting Information Figure S4 shows the DT-CMR maps for a typical volunteer and Figure 9 shows a subject-wise comparison of the corrections at high resolution using E2A, TA, FA, SNR, fraR^2 and R^2. Statistical comparisons were not performed to avoid excessive numbers of statistical tests. E2A, SNR, and the quality measures fraR^2 and R^2 increased and TA decreased towards the values obtained with the standard resolution 2.8mm spiral technique, after both the phase correction and the FSR correction. FA was less affected, but decreased after adding the FSR correction. A combination of phase correction and FSR showed the closest results to the standard resolution data.

T2* correction

Supporting Information Figure S1 demonstrates a significant increase (P=0.002) in sharpness when the T2* correction is added for both resolutions in systole. While the DT-CMR parameters and the quality measures showed no significant changes in E2A (Figure 9) compared to the FSR correction (P=0.11), there was a 9% and 7% increase in TA and FA respectively compared to the FSR reconstruction. The quality measures fraR^2 and R^2 were reduced by 5% and 2% for the T2* correction compared to the FSR reconstruction respectively. The SNR was reduced from 8.11 to 6.66 by adding the T2* correction.

Discussion and Conclusion

This is the first demonstration of an in-vivo human DT-CMR acquisition at a 1.8x1.8mm^2 in-plane resolution and the first use of a segmented DT-CMR technique. A segmented variable density spiral trajectory was used for DT-CMR and a novel field-map acquisition technique using the STEAM sequence was developed and successfully tested. To date the resolution of in-vivo STEAM DT-CMR human studies is typically around 2.8x2.8x8mm^3 (4,11,38–42) with reports of resolutions up to 2.0x2.0x8mm^3 (43). A resolution of 1.6x1.6x10mm^3 (44) was achieved for a second order motion compensated diffusion prepared balanced steady-state free precession (bSSFP) sequence but only three diffusion encoding directions were obtained. Relative to our established EPI sequence with a resolution of 2.8x2.8x8mm^3 the cross-sectional area of each pixel is reduced by 60% with our high resolution spiral sequence and we have demonstrated the increase in image sharpness associated with this increase in spatial resolution.

This work has shown that segmented variable density spiral STEAM acquisitions with the appropriate corrections produces largely similar DT-CMR parameters to a lower resolution STEAM spiral sequence, while the quality of single shot EPI data at the same resolution was poor. The importance of correcting for motion-induced phase between the interleaves was demonstrated, as was correcting for off-

resonance effects during the spiral readout. We also implemented a T2* correction based on an estimated LV T2* value calculated for each subject.

Artefact corrections

Phase and off-resonance corrections

Long spiral readouts are sensitive to field inhomogeneities, resulting in blurring (45) artefacts. In order to increase spatial resolution an interleaved spiral was used. For diffusion weighted images, bulk motion during the diffusion time is encoded in the image phase, which varies between images due to inter-heart beat differences in cardiac motion. In order to correct for these phase differences, variable density spirals were used, providing alias free low resolution data from each interleave for use in the correction. The functionality of this correction was verified and led to an SNR gain of 2.1 compared to the uncorrected equivalent with an SNR=2.2 (Figure 9) and also to improvements in all other quality measures. The resultant change in the DT-CMR parameters is partly a consequence of this improvement in SNR. SNAILS (46) has a very similar approach subtracting the low frequency phase information from each diffusion encoded spiral interleaf, but has never been demonstrated in the heart.

Despite segmenting our spiral acquisitions, our spiral readouts were relatively long (~15ms). In order to reduce the effects of off-resonance induced dephasing during these readouts, we used an FSR with a field map acquired in each breath-hold.

Field maps can be acquired with a gradient echo or with the STEAM sequence as used here. The disadvantage of the novel STEAM field map acquisition sequence is a lower signal intensity and increased complexity compared to a gradient echo sequence. The readout used for off-resonance correction is delayed to allow the prior acquisition of another spiral used to correct the first for motion-induced phase. The delay leads to off-resonance induced phase dispersion related signal loss and reduced SNR in the field maps themselves. However, a gradient echo based field map would not be able to take advantage of the reduced stimulated echo FOV and registration would be required between the field map and image data.

In the preliminary work for this study (unpublished) several off-resonance correction methods were tested and compared. Low order corrections (zero and first order) did not substantially improve the data quality. However, the FSR correction implemented here brought the DT-CMR parameters into the expected range: there were no significant differences between the 2.8x2.8 and the 1.8x1.8 mm^2 FSR and T2* corrected spiral acquisitions except in HAG and FA, which could be due to either or both the reduced SNR and higher spatial resolution. Adding the FSR correction to the high resolution data reconstruction increased the SNR from 4.3 to 8.1 and resulted in substantial increases in the data quality measures fraR^2 and R^2.

T2* correction

A further consequence of the long readout trajectories is blurring due to T2* decay during the readout. In this work we tested a subject-wise T2* correction. For a readout lengths of 15 ms and the LV T2* calculated here of 34ms, the signal intensity at the end of the readout would be attenuated by 36%. As expected, the T2* correction led to a reduction of the SNR from 8.1 to 6.7. The data quality measures fraR^2 and R^2 were slightly reduced; however, the edges were visibly sharper and quantitative sharpness measures were significantly increased. While there were significant differences in HAG, TA and FA for the T2* correction, this could be due to either or both of the reductions in SNR and in

blurring and we hope that this correction can assist in uncovering new detail in myocardial microstructure.

Comparison of the standard to high resolution sequences

While the HAG was similar for all EPI and spiral sequences, the median of the fraR^2 was 0.48 for the high resolution EPI data, which means that more than half of the data was not used in the HAG calculation. The HAG of the spiral high resolution data for both cardiac phases was within one standard deviation of values cited in the literature (40,43,47). E2A and MD showed no significant differences between the spiral sequences for both cardiac phases and values lay within the range stated in the literature (4,5,37,40,42,43,47,48) but the high resolution EPI sequence did not provide comparable results to the standard resolution sequence. FA showed significantly higher results for the high resolution data for all sequences; however, FA depends on both the SNR and the spatial resolution. A reduction in SNR can result in an increase in FA via eigenvalue repulsion (26,49), but the range of microstructural angles contained within each voxel is also reduced with increasing resolution (described as dispersion in DT neuroimaging).

The measured SNR is higher for the spiral sequences when compared to the equivalent EPI sequences, which was also demonstrated in (47). Relative to the standard resolution, the SNR decreases by 63%, 29% and 36% for the high resolution EPI, systolic and diastolic spiral respectively. The large decrease in SNR of the high resolution EPI data relative to the standard resolution is largely due to the long TE required for this sequence. Assuming T2=47ms (50) the 13ms TE increase between the standard resolution spiral and EPI sequences results in a signal reduction of 24%, while the TE increase of 32ms required for the longer readout of the high resolution EPI compared to high resolution spiral results in a signal reduction by 49%. This study suggests that the SNR available with the 1.8x1.8x8mm^3 STEAM EPI sequence used here is not sufficient for DT-CMR data acquisition.

The echo time of the spiral sequences does not depend on spatial resolution. For the spiral technique in systole, the SNR of the high resolution data is comparable with the SNR of the standard resolution data using EPI (6.7 vs. 6.5, high resolution spiral vs. standard resolution EPI).

In addition to comparing the high resolution spiral acquisitions to the standard resolution data with the same number of averages, we also performed spiral reconstructions with half the number of averages, therefore matching the number of breath-holds used in the tensor calculated with the standard resolution acquisitions. All DT-CMR parameters except FA were similar between the equivalent NM and TM acquisitions. The higher FA values (0.49/0.61 systole/diastasis) obtained with the TM reconstruction compared to the NM reconstruction (0.47/0.59 systole/diastasis), are likely to be a consequence of eigenvalue repulsion effects (49). For the systolic acquisition, the quality measures are suggestive of poorer quality data when going from the NM to TM reconstructions (significantly higher %negEV, stdTA and lower R^2) and the interquartile ranges are larger using TM. For the diastolic acquisitions, all quality measures except the %negEV were not significantly different between the NM and TM data. While in some subjects and some cardiac phases, the TM data was sufficient to reconstruct a similar quality set of DT-CMR parameter maps to the NM data, in others more averages were required. Future studies on the optimal number of averages for a given acquisition scheme (51) and on-the-fly calculation of the DT-CMR parameter maps may be of particular use for the high resolution spiral sequence proposed here.

Study limitations and future work

In this study we compared a segmented spiral sequence to a single shot EPI sequence. An interleaved EPI sequence could reduce TE to values similar to the standard resolution EPI sequence and would, therefore increase the SNR and possibly image quality. Off-resonance and T2* corrections, as were performed on the spiral data, could potentially increase the quality of the EPI data. Nevertheless, the geometry of a spiral is well suited to segmented acquisitions and the variable density spirals allow a straightforward correction for the motion-induced phase. Furthermore, the inherent loss of SNR with increased spatial resolution is partially mitigated by the increased SNR available with the short spiral TE.

Although the T2* correction sharpens the images, it also increases the noise by adding weight to high spatial frequencies. Furthermore, the T2* value is calculated from the whole FOV and the T2*decay is likely underestimated (52).

The proposed sequence depends on subjects holding their breath. In particular, during the beginning of the breath-hold, as bulk motion results in an inaccurate estimation of the field map, this in turn corrupts the DW images during the off-resonance correction. This is, however, also a problem for the STEAM EPI sequence where EPI phase correction and parallel imaging reference data is acquired at the beginning of the breath-hold. In order to avoid cardiac disease history, most volunteers were relatively young. However, 5 of the 10 subjects were having their first CMR scan, therefore reducing the “expert volunteer” bias. A small number of images acquired with both spiral and EPI sequences show off resonance related signal loss in the inferolateral wall.

During this study, the in-plane resolution was increased but the slice-thickness was the same as that used in previous studies. In future work super-resolution applied to multi slice acquisitions or 3D acquisitions could be investigated to reduce the effective slice thickness (53).

In future work an online reconstruction of the spiral sequence will be implemented and alternative off-resonance correction methods, including conjugate phase reconstruction (54) will be investigated. The long acquisition time to acquire a sufficient number of averages (double number of breath-holds for same number of averages) for a robust tensor reconstruction could be reduced through parallel imaging (subject to SNR loss) or compressed-sensing techniques (55–57). Further sequence refinements may include optimising the spatial resolution of the field-map spirals and making use of multiple echo times when calculating the field maps or by not acquiring the additional ΔTE_{FM}=0 or ΔTE_{FM}=3ms images which were unused here, therefore matching the breath-hold duration to the EPI sequence. The most important test of this sequence will be in patient cohorts with a thinned myocardium or focal disease, for example in patients with chronic myocardial infarction or in the right ventricle, where the benefit of the increased spatial resolution will be needed.

Conclusion

In-plane spatial resolution of STEAM DT-CMR data can be increased substantially by using an interleaved variable density spiral trajectory, when motion-induced phase is taken into account. The additional myocardial SNR provided by the short TE of the spiral trajectory is traded for increased resolution. T2* decay and off-resonance effects during the spiral readout can be corrected and we have introduced a novel method for calculating a field map from STEAM acquisitions with a spiral readout. While this high resolution spiral DT-CMR method was able to acquire good quality data at 1.8x1.8mm^2 in-plane resolution, a single shot EPI sequence with matched spatial resolution produced lower quality DT-CMR data. This reduction in pixel volume of 60% may be of use in patients with focal disease, thinned myocardium and in the right ventricle.

Table 1: Used sequence parameter

	EPI (2.8mm)	EPI (1.8mm)	Single shot spiral (2.8mm)	Interleaved spiral (1.8mm)
Cardiac phase	systole	systole	systole/diastasis	systole/diastasis
TE [ms]	24	43	11	11
Readout duration [ms]	12	31	15	15
Stimulated echo FOV [mm^2]	360x135	350x120	96x96	96x96
Readout FOV [mm^2]	360x135	350x120	120x120	190-110x 190-110
Reconstructed FOV [mm^2]	360x135	350x120	120x120	120x120
Dwell time [µs]	1.6	1.4	2.8	2.8
Number of acquisitions b_{ref}/b_{main}	2/8	2/16	2/8	1/8
Parallel imaging	SENSE x2	SENSE x2	-	-
Acquired/reconstructed resolution [mm^3]	2.8x2.8x8/ 1.4x1.4x8	1.8x1.8x8/ 0.9x0.9x8	2.8x2.8x8/ 1.4x1.4x8	1.8x1.8x8/ 0.9x0.9x8

Figures

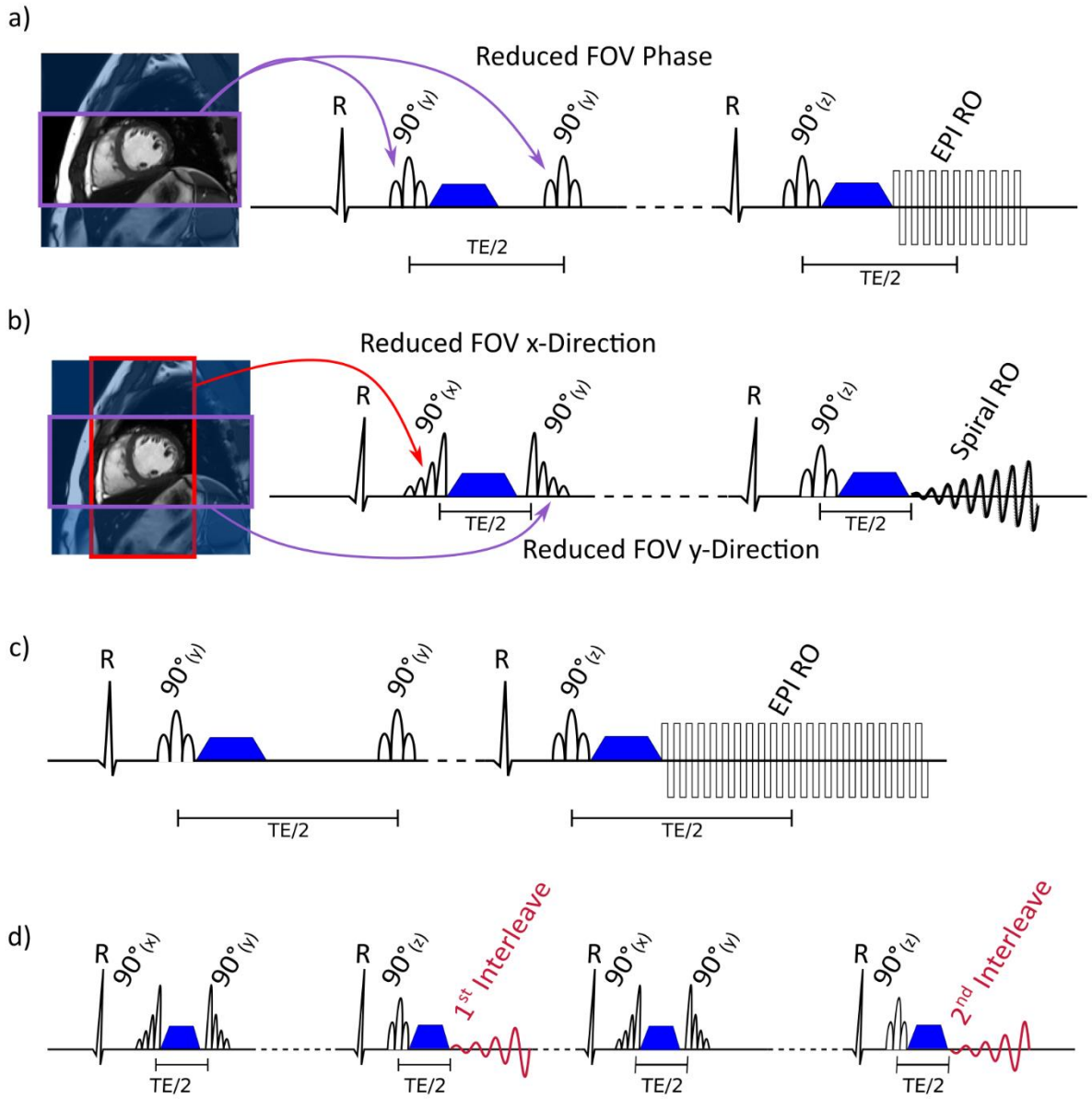


Figure 1: The sequences used. a) STEAM EPI sequence with a reduced FOV in phase direction, used to acquire standard resolution DT-CMR images. b) Single shot spiral STEAM sequence. The FOV is reduced in both the x and y direction. The sequence was used to acquire standard resolution DT-CMR data. c) High resolution single shot STEAM EPI sequence. The sequence matches sequence a) but to obtain a higher resolution, TE is increased. d) Segmented variable density spiral STEAM sequence. The sequence runs over four consecutive cardiac cycles. Sequences c) and d) were used to acquire high resolution DT-CMR data. Chemical-shift selective fat suppression is applied before each STEAM initial excitation for all sequences (not shown).

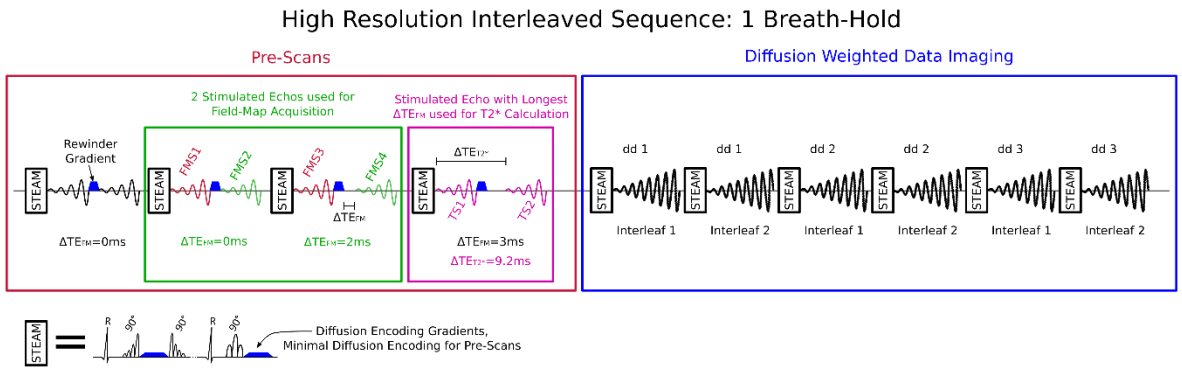


Figure 2: A schematic showing a single breath-hold for the high resolution data acquisition. The pre-scans (red box) consist of 8 cardiac cycles with 4 stimulated echoes, of which 2 are used for the field-map acquisition (green box) and 1 for the T2* estimation (magenta box). Diffusion weighted data is acquired in 12 cardiac cycles and 6 stimulated echoes (blue box). For a standard resolution sequence, 6 diffusion directions (dd) with 1 stimulated echo each are acquired.

Four cardiac cycles with two stimulated echoes (green box) are used for the field map acquisition. A field map calculation needs (at least) two readouts at different echo times. Here the green readouts FMS2 and FMS4 with a difference in echo time of ΔTE_{FM} are used. The phase of these readouts is a sum of the motion induced phase, as a consequence of signal acquisitions in different echoes, and the off-resonance related dephasing. The motion-induced phase is estimated as the phase differences between the red readouts FMS1 and FMS3. These phase differences are then used to correct the readout FMS4. After the correction, the field map can be calculated. The LV T2* is estimated from the readouts TS1 and TS2, the readouts with the longest ΔTE.

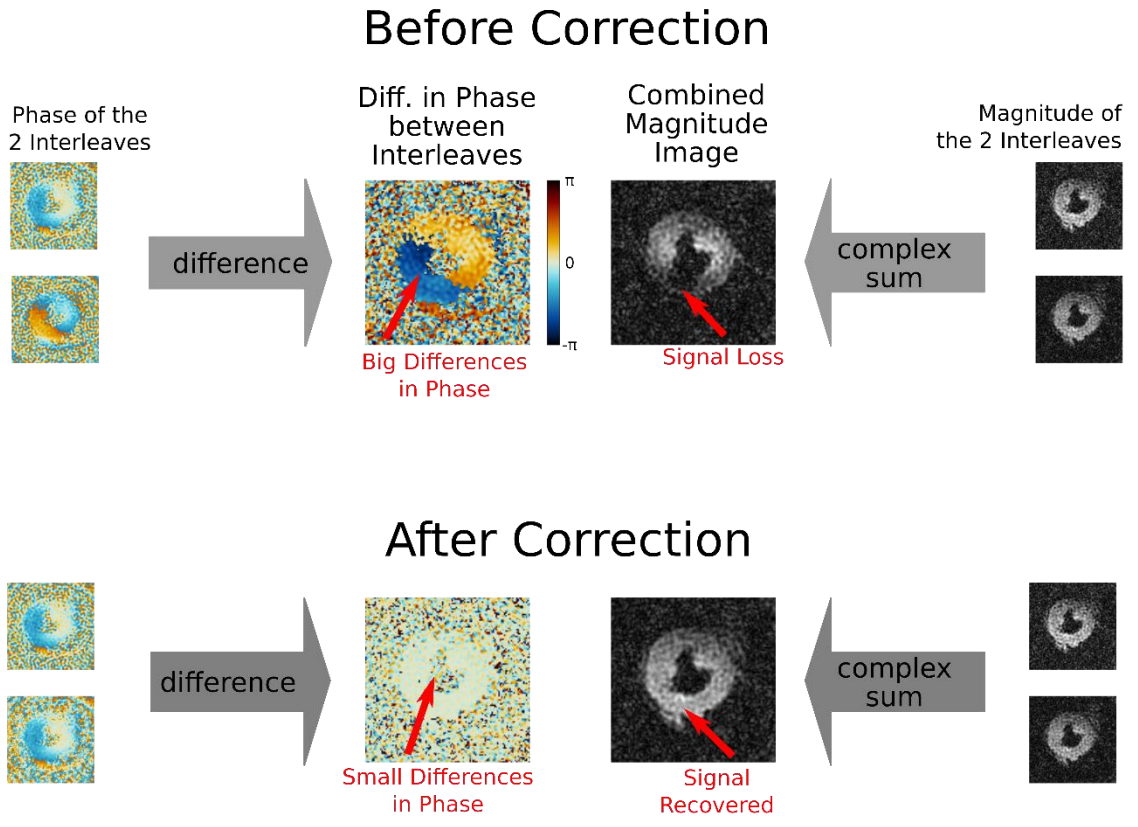


Figure 3: Spiral interleaves acquired in different cardiac cycles have differing bulk motion induced phase (top left). When the interleaves are combined in complex space, this leads to signal drop out. During the motion induced phase correction, the phase of the second interleave is corrected to be similar to the first and the signal is recovered.

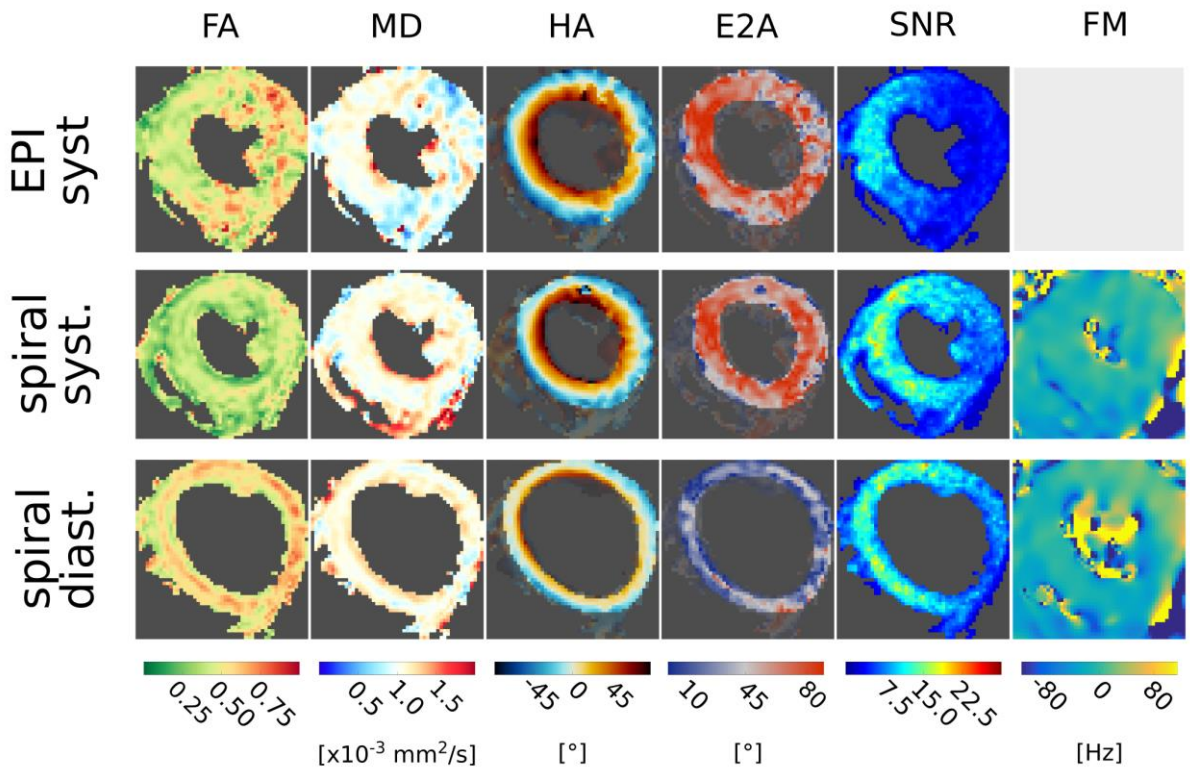


Figure 4: Fractional anisotropy (FA), mean diffusivity (MD), helix angle (HA), secondary eigenvector angulation (E2A), signal to noise ratio (SNR) and field maps (FM) are shown for the EPI and spiral sequences performed at 2.8x2.8mm^2. Spiral data is shown with all artefact corrections applied. The differences in SNR over the myocardium in both EPI and spiral sequences is predominantly caused by the variation in distance to the receiver coils and a variable degree of off-resonance artefacts.

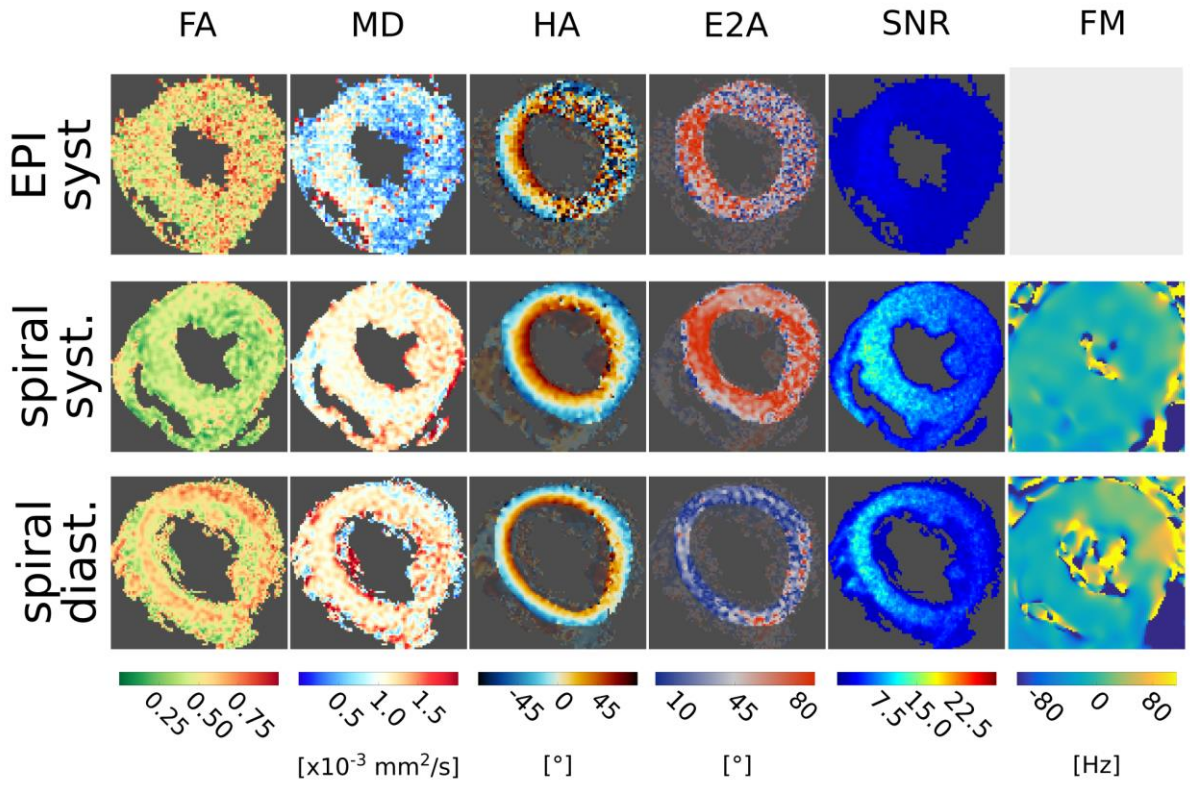


Figure 5: The high resolution (1.8x1.8mm^2) DT-CMR results for the same subject as shown in Figure 4.

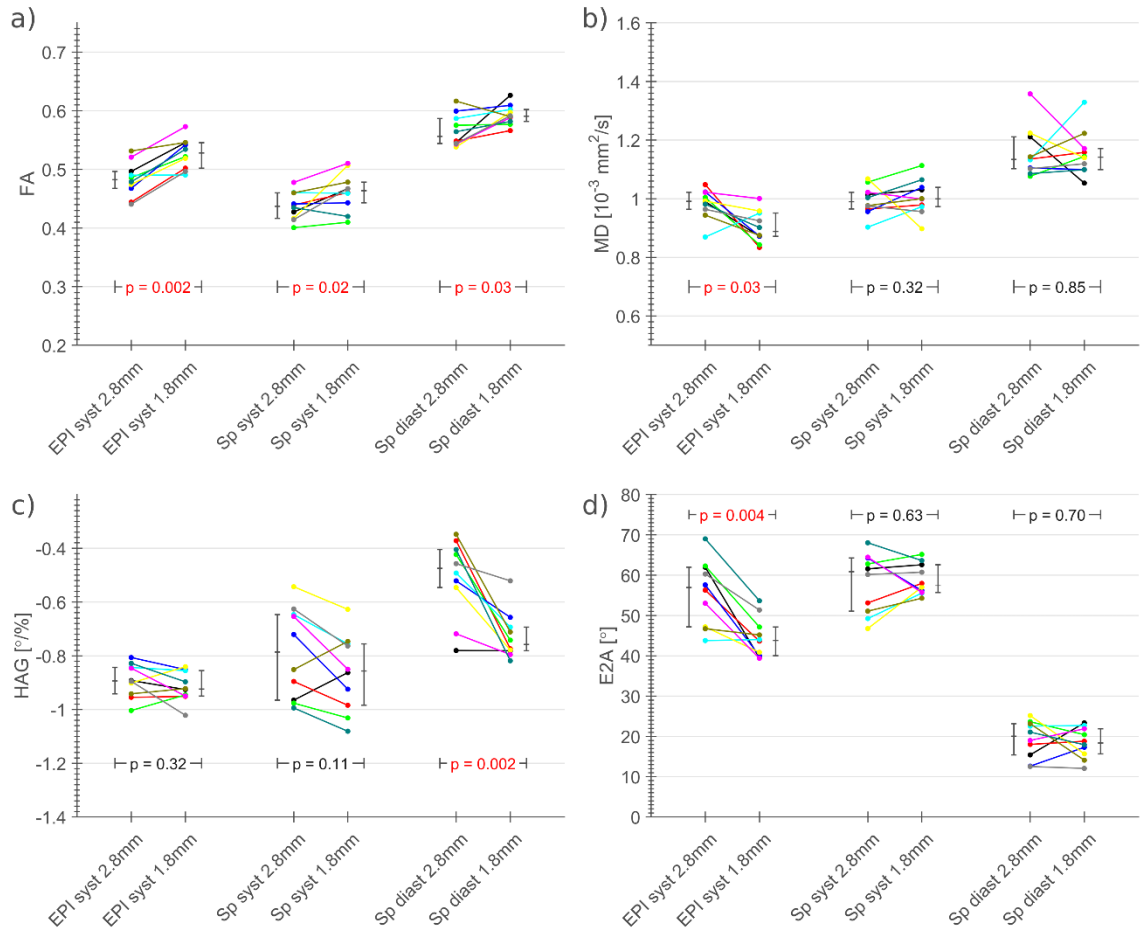


Figure 6: Subject-wise comparison of FA (a), MD (b), HAG (c) and E2A (d). The medians and interquartile ranges are plotted in black. The individual subjects are colour-coded consistently in all figures. A Wilcoxon signed-rank test was calculated between the standard and high resolution data of the same readout technique in the same cardiac phase. P<0.05 was considered significant.

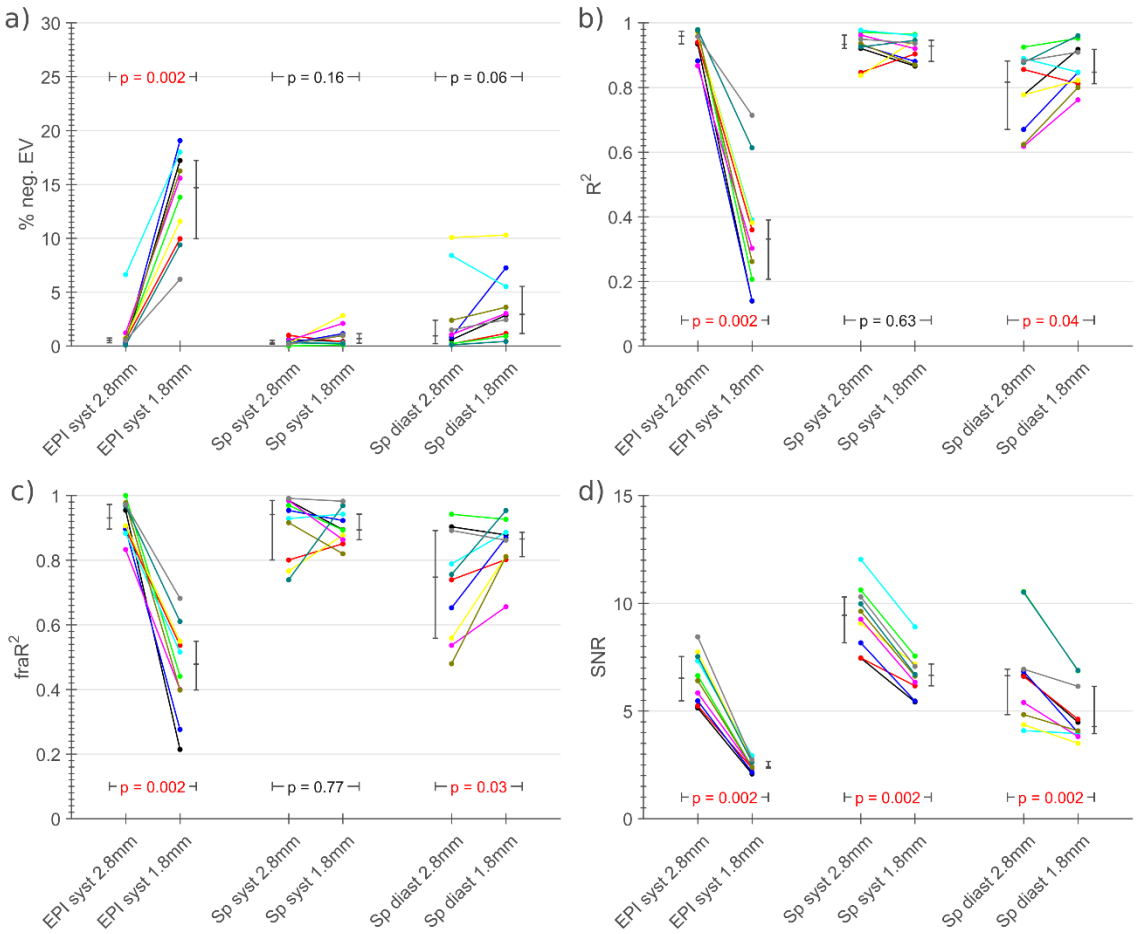


Figure 7: Subject-wise comparison of the data quality using %negEV, R^2, $fraR^2$ and SNR measures.

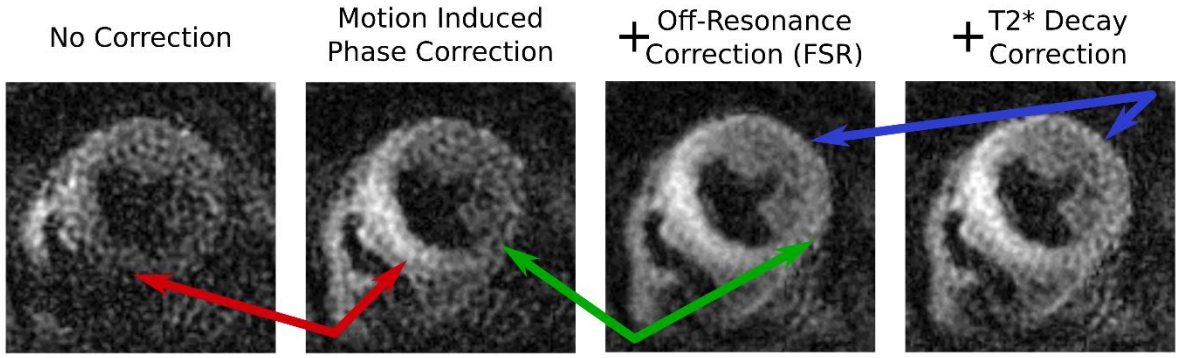


Figure 8: A comparison of the reconstruction methods added stepwise, i.e. each additional correction is added to the previous corrections. The motion induced phase correction recovered the signal in the septal wall (red arrow) compared to the not corrected reconstruction; the frequency segmented reconstruction (FSR) correction recovered further signal in the lateral wall (green arrow) and the T2* correction sharpened the edges of the myocardium (blue arrow).

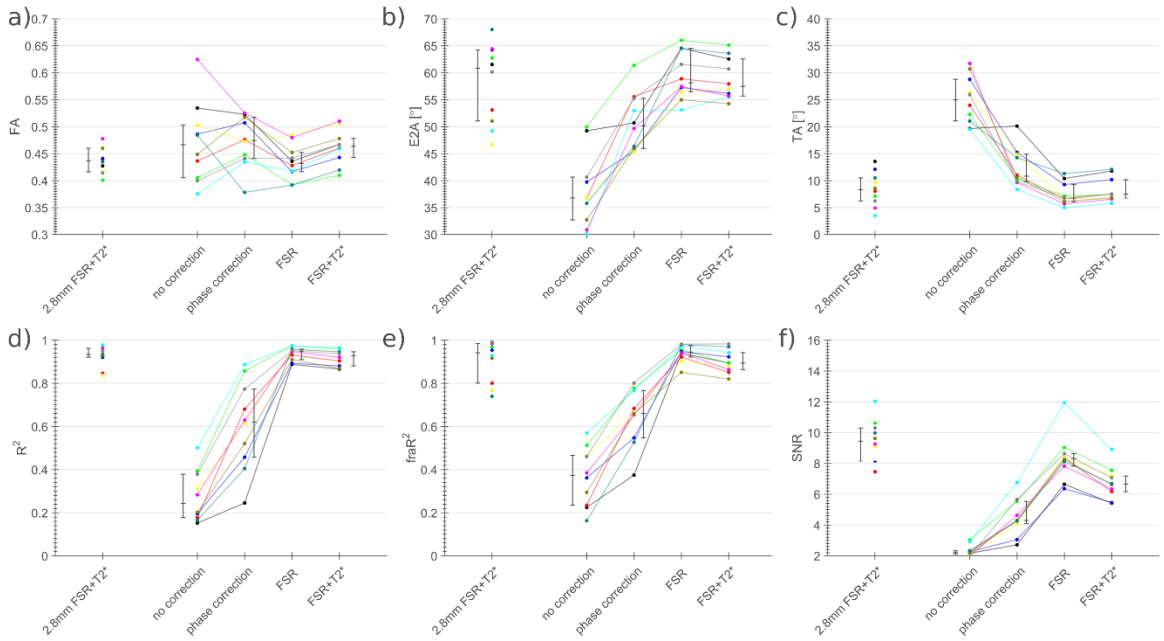
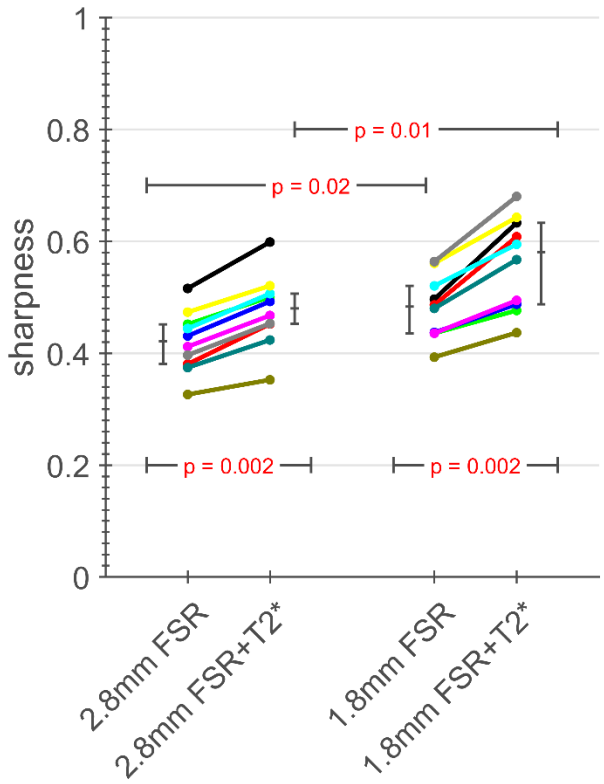
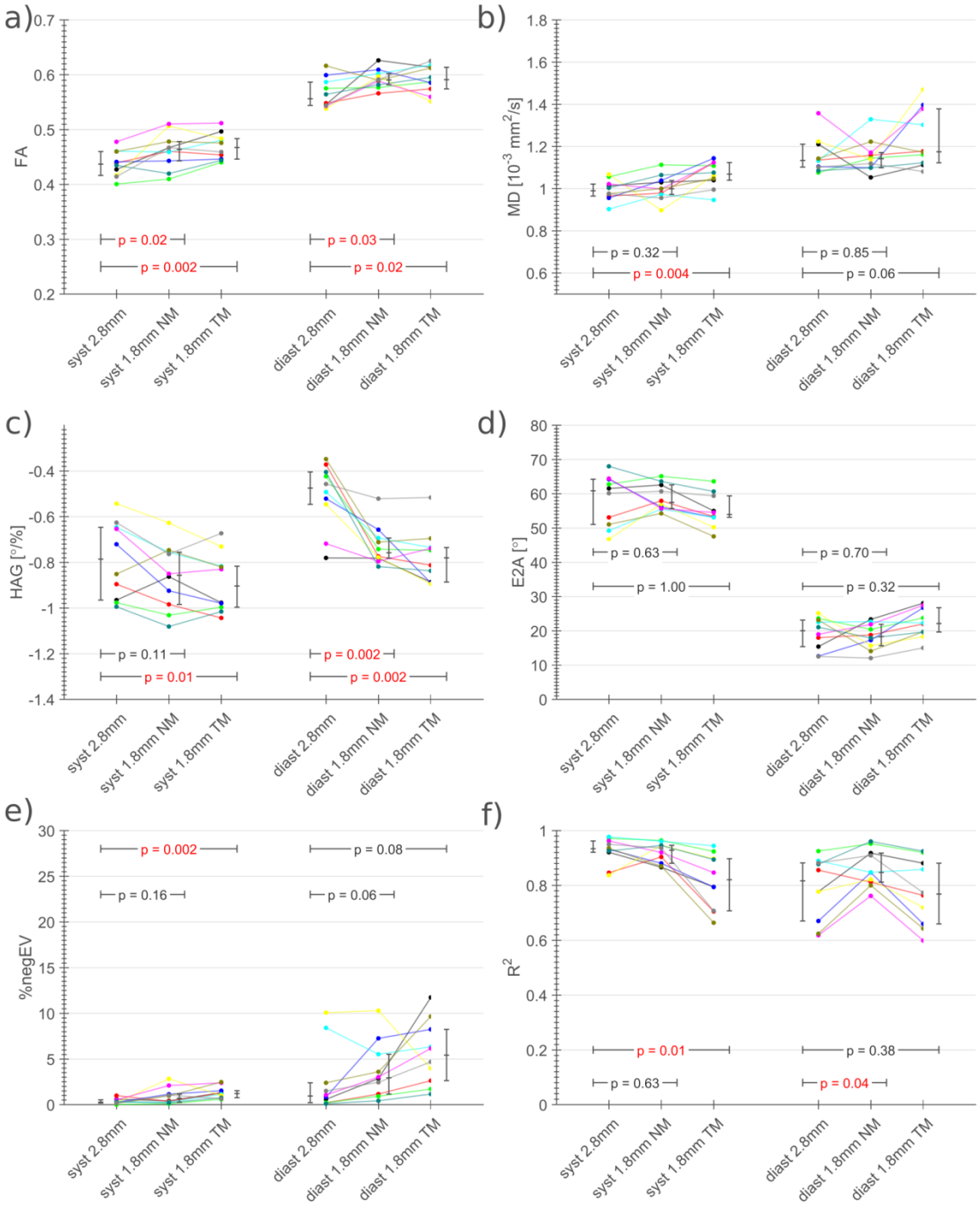


Figure 9: Subject-wise comparison of the different reconstruction techniques is shown for FA (a), E2A (b), TA (c), R^2 (d), fraR^2 (e) and SNR (f). The standard resolution spiral data are also plotted for comparison.

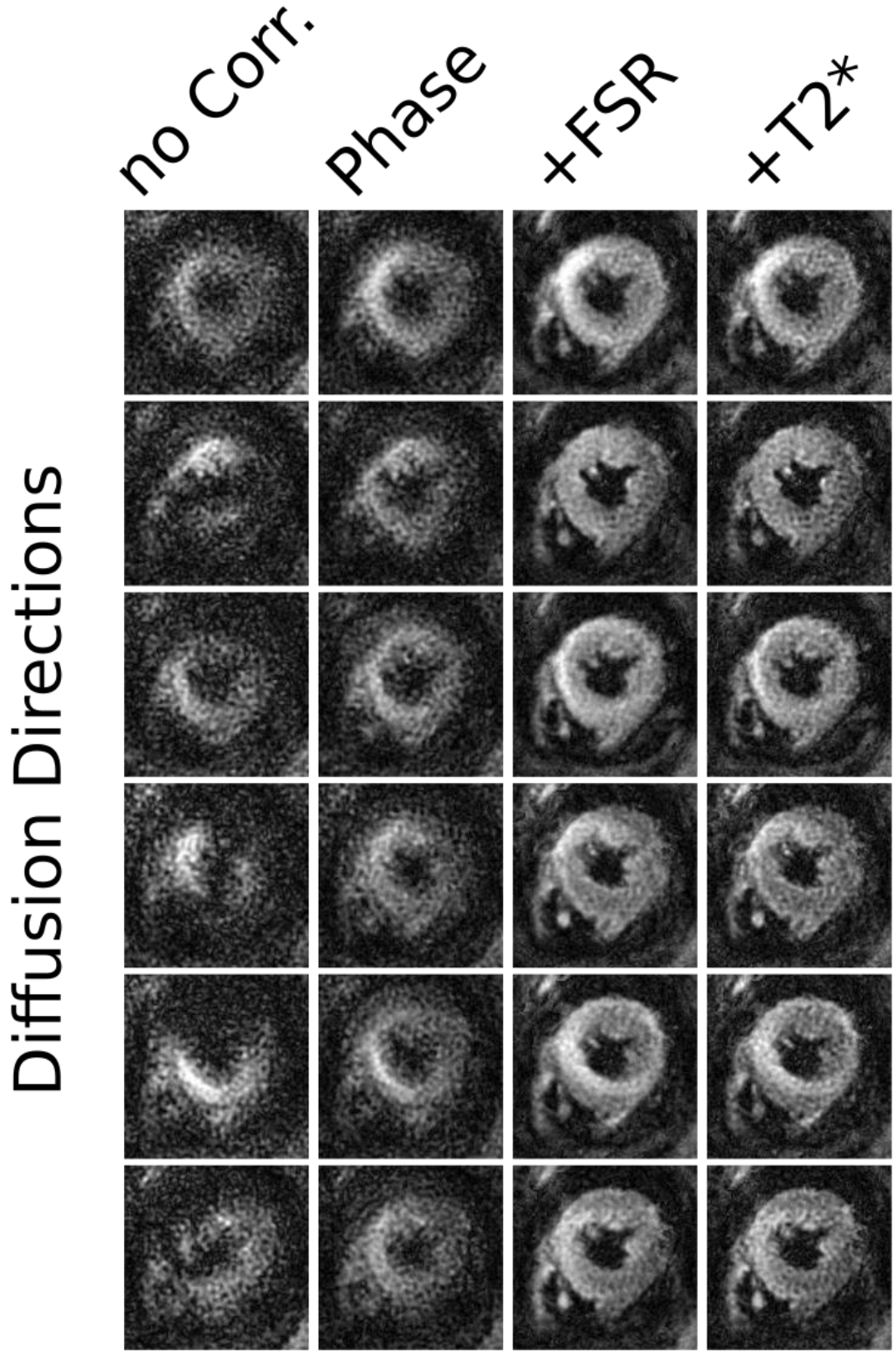
Supporting Information:



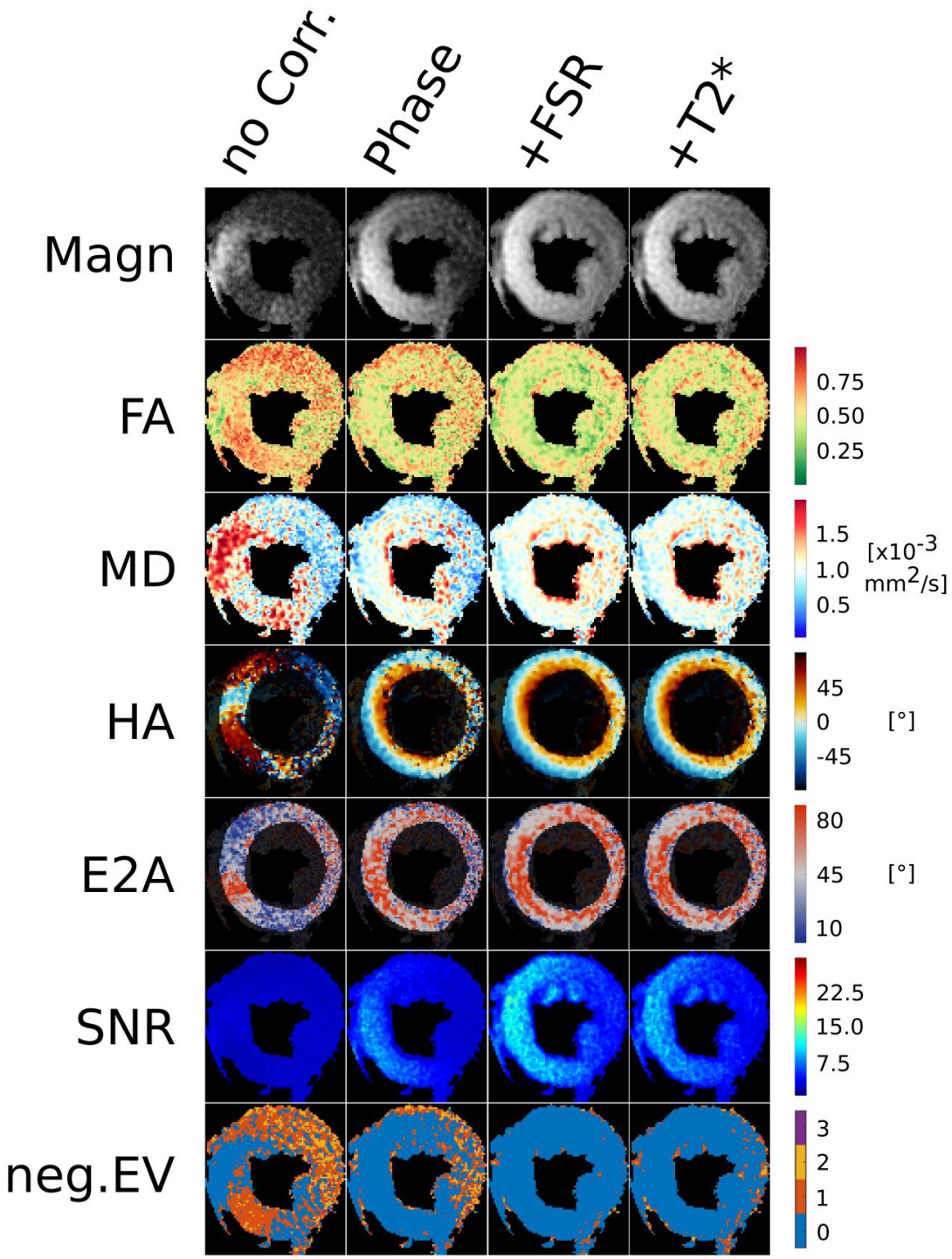
Supporting Information Figure S1: Comparison of the sharpness measurement for the standard and high resolution systolic spiral data for the FSR and FSR+T2* reconstructions.



Supporting Information Figure S2: The number matched (NM) and time matched (TM) reconstructions for systole (syst) and diastole (diast) are compared. FA (a), MD (b), HAG (c), E2A (d), %negEV (e) and R^2 (f) are shown.



Supporting Information Figure S3: A set of 6 different diffusion encoding directions at a resolution of 1.8x1.8mm^2. Reconstructed without a correction (corr.) (left), then showing the effect of successively adding motion induced phase correction, FSR and T2* correction.



Supporting Information Figure S4: A comparison of reconstructions with different correction methods applied. One can see how the data quality improves for the estimated magnitude image for (b=0s/mm^2), E2A, HA, MD, FA, SNR and negEV maps. The reconstructions without a correction, with phase correction, with added FSR off-resonance correction and with added T2* correction are compared. Note that blood pool and epicardial signal masks are applied to each dataset based on the FSR corrected data, which result in the uncorrected and phase corrected data looking sharper here than in the unmasked data.

		EPI	spiral systole	spiral diastasis
FA	**2.8mm**	0.48 ± 0.03	0.44 ± 0.04	0.56 ± 0.04
	1.8mm NM	0.53 ± 0.04	0.46 ± 0.04	0.59 ± 0.02
	1.8mm TM		0.48 ± 0.04	0.59 ± 0.04
MD [x10^{-3} mm^2/s]	**2.8mm**	0.99 ± 0.06	0.99 ± 0.06	1.13 ± 0.11
	1.8mm NM	0.89 ± 0.08	1.00 ± 0.07	1.14 ± 0.07
	1.8mm TM		1.08 ± 0.08	1.17 ± 0.26
HAG [°/%]	**2.8mm**	-0.89 ± 0.10	-0.79 ± 0.32	-0.47 ± 0.14
	1.8mm NM	-0.92 ± 0.09	-0.86 ± 0.23	-0.76 ± 0.09
	1.8mm TM		-0.98 ± 0.18	-0.78 ± 0.15
E2A [°]	**2.8mm**	57 ± 15	61 ± 13	20 ± 8
	1.8mm NM	44 ± 7	57 ± 7	18 ± 6
	1.8mm TM		53 ± 4	22 ± 7
%negEV	**2.8mm**	0.5 ± 0.4	0.3 ± 0.3	0.9 ± 2.2
	1.8mm NM	14.7 ± 7.3	0.7 ± 0.9	2.9 ± 4.4
	1.8mm TM		1.3 ± 0.8	5.4 ± 5.6
R^2	**2.8mm**	0.93 ± 0.08	0.94 ± 0.18	0.75 ± 0.33
	1.8mm NM	0.48 ± 0.15	0.89 ± 0.08	0.87 ± 0.08
	1.8mm TM		0.80 ± 0.11	0.77 ± 0.22
fraR^2	**2.8mm**	0.93 ± 0.08	0.94 ± 0.18	0.75 ± 0.33
	1.8mm NM	0.48 ± 0.15	0.89 ± 0.08	0.87 ± 0.08
	1.8mm TM		0.80 ± 0.11	0.74 ± 0.16
SNR	**2.8mm**	6.5 ± 2.1	9.4 ± 2.1	6.6 ± 2.1
	1.8mm	2.4 ± 0.3	6.7 ± 1.0	4.3 ± 2.2

Supporting Information Table S1: The mean and the interquartile ranges are summarised for the main DT-CMR results and quality measures.

References

1. Dou J, Tseng WI, Reese TG, Wedeen VJ. Combined diffusion and strain MRI reveals structure and function of human myocardial laminar sheets in vivo. Magn. Reson. Med. 2003;50:107–113.
2. Edelman RR, Gaa J, Wedeen VJ, Loh E, Hare JM, Prasad P, Li W. In vivo measurement of water diffusion in the human heart. Magn. Reson. Med. 1994;32:423–428.
3. Reese TG, Weisskoff RM, Smith RN, Rosen BR, Dinsmore RE, Wedeen VJ. Imaging myocardial fiber architecture in vivo with magnetic resonance. Magn. Reson. Med. 1995;34:786–791.
4. Nielles-Vallespin S, Khalique Z, Ferreira PF, de Silva R, Scott AD, Kilner P, McGill L-A, Giannakidis A, Gatehouse PD, Ennis D. Assessment of myocardial microstructural dynamics by in vivo diffusion tensor cardiac magnetic resonance. J. Am. Coll. Cardiol. 2017;69:661–676.
5. Ferreira PF, Kilner PJ, McGill L-A, Nielles-Vallespin S, Scott AD, Ho SY, McCarthy KP, Haba MM, Ismail TF, Gatehouse PD. In vivo cardiovascular magnetic resonance diffusion tensor imaging shows evidence of abnormal myocardial laminar orientations and mobility in hypertrophic cardiomyopathy. J. Cardiovasc. Magn. Reson. 2014;16:1.
6. Nguyen C, Fan Z, Xie Y, Dawkins J, Tseliou E, Bi X, Sharif B, Dharmakumar R, Marbán E, Li D. In vivo contrast free chronic myocardial infarction characterization using diffusion-weighted cardiovascular magnetic resonance. J. Cardiovasc. Magn. Reson. [Internet] 2014;16:1.
7. Nguyen C, Lu M, Fan Z, Bi X, Kellman P, Zhao S, Li D. Contrast-free detection of myocardial fibrosis in hypertrophic cardiomyopathy patients with diffusion-weighted cardiovascular magnetic resonance. J. Cardiovasc. Magn. Reson. 2015;17:1.
8. Wu M-T, Tseng W-YI, Su M-YM, Liu C-P, Chiou K-R, Wedeen VJ, Reese TG, Yang C-F. Diffusion tensor magnetic resonance imaging mapping the fiber architecture remodeling in human myocardium after infarction correlation with viability and wall motion. Circulation [Internet] 2006;114:1036–1045.
9. Wu M-T, Su M-YM, Huang Y-L, Chiou K-R, Yang P, Pan H-B, Reese TG, Wedeen VJ, Tseng W-YI. Sequential changes of myocardial microstructure in patients postmyocardial infarction by diffusion-tensor cardiac MR correlation with left ventricular structure and function. Circ. Cardiovasc. Imaging [Internet] 2009;2:32–40.
10. Hales PW, Schneider JE, Burton RAB, Wright BJ, Bollensdorff C, Kohl P. Histo-anatomical structure of the living isolated rat heart in two contraction states assessed by diffusion tensor MRI. Prog. Biophys. Mol. Biol. [Internet] 2012;110:319–330.
11. Nielles-Vallespin S, Mekkaoui C, Gatehouse P, Reese TG, Keegan J, Ferreira PF, Collins S, Speier P, Feiweier T, Silva R. In vivo diffusion tensor MRI of the human heart: Reproducibility of breath-hold and navigator-based approaches. Magn. Reson. Med. 2013;70:454–465.
12. Frost R, Miller KL, Tijssen RHN, Porter DA, Jezzard P. 3D multi-slab diffusion-weighted readout-segmented EPI with real-time cardiac-reordered k-space acquisition. Magn. Reson. Med. 2014;72:1565–1579. doi: 10.1002/mrm.25062.
13. Chen N, Guidon A, Chang H-C, Song AW. A robust multi-shot scan strategy for high-resolution diffusion weighted MRI enabled by multiplexed sensitivity-encoding (MUSE). Neuroimage 2013;72:41–47.
14. Wang Y, Ma X, Zhang Z, Dai E, Jeong HK, Xie B, Yuan C, Guo H. A comparison of readout segmented EPI and interleaved EPI in high-resolution diffusion weighted imaging. Magn. Reson. Imaging [Internet] 2018;47:39–47. doi: 10.1016/j.mri.2017.11.011.
15. Holdsworth SJ, Skare S, Newbould RD, Guzmann R, Blevins NH, Bammer R. Readout-segmented EPI for rapid high resolution diffusion imaging at 3T. Eur. J. Radiol. 2008;65:36–46. doi: 10.1016/j.ejrad.2007.09.016.
16. Nguyen C, Fan Z, Xie Y, Pang J, Speier P, Bi X, Kobashigawa J, Li D. In vivo diffusion-tensor MRI of the human heart on a 3 tesla clinical scanner: An optimized second order (M2) motion compensated diffusion-preparation approach. Magn. Reson. Med. 2016;76:1354–1363. doi: 10.1002/mrm.26380.
17. Butts K, de Crespigny A, Pauly JM, Moseley M. Diffusion-weighted interleaved echo-planar imaging with a pair of orthogonal navigator echoes. Magn. Reson. Med. 1996;35:763–770.
18. De Crespigny AJ, Marks MP, Enzmann DR, Moseley ME. Navigated diffusion imaging of normal and

ischemic human brain. Magn. Reson. Med. 1995;33:720–728.
19. Anderson AW, Gore JC. Analysis and correction of motion artifacts in diffusion weighted imaging. Magn. Reson. Med. 1994;32:379–387.
20. Pipe JG. Motion correction with PROPELLER MRI: application to head motion and free-breathing cardiac imaging. Magn. Reson. Med. 1999;42:963–969.
21. Liu C, Bammer R, Kim D, Moseley ME. Self-navigated interleaved spiral (SNAILS): application to high-resolution diffusion tensor imaging. Magn. Reson. Med. [Internet] 2004;52:1388–1396.
22. Tseng WI, Dou J, Reese TG, Wedeen VJ. Imaging myocardial fiber disarray and intramural strain hypokinesis in hypertrophic cardiomyopathy with MRI. J. Magn. Reson. imaging 2006;23:1–8.
23. Gorodezky M, Scott AD, Ferreira PF, Nielles-Vallespin S, Pennell DJ, Firmin DN. Diffusion tensor cardiovascular magnetic resonance with a spiral trajectory: An in vivo comparison of echo planar and spiral stimulated echo sequences. Magn. Reson. Med. [Internet] 2018;80(2):648–54. doi: 10.1002/mrm.27051.
24. Feinberg DA, Hoenninger JC, Crooks LE, Kaufman L, Watts JC, Arakawa M. Inner volume MR imaging: technical concepts and their application. Radiology 1985;156:743–747.
25. Wargo CJ, Moore J, Gore JC. A comparison and evaluation of reduced-FOV methods for multi-slice 7 T human imaging. Magn. Reson. Imaging 2013;31:1349–1359.
26. Scott AD, Nielles-Vallespin S, Ferreira PF, McGill L, Pennell DJ, Firmin DN. The effects of noise in cardiac diffusion tensor imaging and the benefits of averaging complex data. NMR Biomed. [Internet] 2016;29:588–599.
27. Spielman DM, Pauly JM, Meyer CH. Magnetic resonance fluoroscopy using spirals with variable sampling densities. Magn. Reson. Med. 1995;34:388–394.
28. Moriguchi H, Dale BM, Lewin JS, Duerk JL. Block regional off-resonance correction (BRORC): A fast and effective deblurring method for spiral imaging. Magn. Reson. Med. 2003;50:643–648.
29. Scott AD, Ferreira PF, Nielles-Vallespin S, Gatehouse P, McGill L, Kilner P, Pennell DJ, Firmin DN. Optimal diffusion weighting for in vivo cardiac diffusion tensor imaging. Magn. Reson. Med. [Internet] 2015;74:420–430.
30. Hargreaves BA. Variable-Density Spiral Design Functions, http://mrsrl.stanford.edu/~brian/vdspiral/.
31. Fessler JA, Sutton BP. Nonuniform fast Fourier transforms using min-max interpolation. IEEE Trans. Signal Process. [Internet] 2003;51:560–574.
32. Fessler JALB. Michigan Image Reconstruction Toolbox (MIRT). 2017.
33. Roemer PB, Edelstein WA, Hayes CE, Souza SP, Mueller OM. The NMR phased array. Magn. Reson. Med. [Internet] 1990;16:192–225.
34. Ferreira PF, Nielles-Vallespin S, Scott AD, de Silva R, Kilner PJ, Ennis DB, Auger DA, Suever JD, Zhong X, Spottiswoode BS. Evaluation of the impact of strain correction on the orientation of cardiac diffusion tensors with in vivo and ex vivo porcine hearts. Magn. Reson. Med. 2018;79:2205–2215.
35. Reeder SB, Wintersperger BJ, Dietrich O, Lanz T, Greiser A, Reiser MF, Glazer GM, Schoenberg SO. Practical approaches to the evaluation of signal-to-noise ratio performance with parallel imaging: Application with cardiac imaging and a 32-channel cardiac coil. Magn. Reson. Med. [Internet] 2005;54:748–754.
36. Ahmad R, Ding Y, Simonetti OP. Edge sharpness assessment by parametric modeling: Application to magnetic resonance imaging. Concepts Magn. Reson. Part A 2015;44:138–149.
37. Von Deuster C, Stoeck CT, Genet M, Atkinson D, Kozerke SLB. Spin echo versus stimulated echo diffusion tensor imaging of the in vivo human heart. Magn. Reson. Med. 2015.
38. Gorodezky M, Scott AD, Ferreira P, Nielles-Vallespin S, Khalique Z, Pennell D, Firmin D. In-vivo comparison of STEAM EPI and STEAM spiral diffusion-weighted sequences. In: International Society for Magnetic Resonance in Medicine Annual Meeting. Honolulu, USA; 2017.
39. Scott AD, Nielles-Vallespin S, Ferreira PF, Khalique Z, Gatehouse PD, Kilner P, Pennell DJ, Firmin DN. An in-vivo comparison of stimulated-echo and motion compensated spin-echo sequences for 3 T diffusion tensor cardiovascular magnetic resonance at multiple cardiac phases. J. Cardiovasc.

Magn. Reson. [Internet] 2018;20:1. doi: 10.1186/s12968-017-0425-8.
40. McGill LA, Ferreira PF, Scott AD, Nielles-Vallespin S, Giannakidis A, Kilner PJ, Gatehouse PD, De Silva R, Firmin DN, Pennell DJ. Relationship between cardiac diffusion tensor imaging parameters and anthropometrics in healthy volunteers. J. Cardiovasc. Magn. Reson. [Internet] 2016;18:1.
41. McGill L-A, Scott AD, Ferreira PF, Nielles-Vallespin S, Ismail T, Kilner PJ, Gatehouse PD, de Silva R, Prasad SK, Giannakidis A. Heterogeneity of fractional anisotropy and mean diffusivity measurements by in vivo diffusion tensor imaging in normal human hearts. PLoS One 2015;10:e0132360.
42. Tunnicliffe EM, Scott AD, Ferreira P, Ariga R, McGill L-A, Nielles-Vallespin S, Neubauer S, Pennell DJ, Robson MD, Firmin DN. Intercentre reproducibility of cardiac apparent diffusion coefficient and fractional anisotropy in healthy volunteers. J. Cardiovasc. Magn. Reson. [Internet] 2014;16:1.
43. Stoeck CT, Kalinowska A, von Deuster C, Harmer J, Chan RW, Niemann M, Manka R, Atkinson D, Sosnovik DE, Mekkaoui C. Dual-phase cardiac diffusion tensor imaging with strain correction. PLoS One [Internet] 2014;9:e107159.
44. Nguyen C, Fan Z, Sharif B, He Y, Dharmakumar R, Berman DS, Li D. In vivo three-dimensional high resolution cardiac diffusion-weighted MRI: A motion compensated diffusion-prepared balanced steady-state free precession approach. Magn. Reson. Med. 2014;72:1257–1267. doi: 10.1002/mrm.25038.
45. Yudilevich E, Stark H. Spiral sampling in magnetic resonance imaging-the effect of inhomogeneities. IEEE Trans. Med. Imaging 1987;6:337–345.
46. Liu C, Bammer R, Kim DH, Moseley ME. Self-navigated interleaved spiral (SNAILS): Application to high-resolution diffusion tensor imaging. Magn. Reson. Med. 2004;52:1388–1396. doi: 10.1002/mrm.20288.
47. Gorodezky M, Ferreira P, Scott AD, Nielles-Vallespin S, Pennell D, Firmin D. A comparison of spiral and EPI trajectories for in-vivo cardiac DTI. In: Society for Cardiovascular Magnetic Resonance 20th Annual Scientific Sessions. Washington DC, USA; 2017.
48. Nielles-Vallespin S, Mekkaoui C, Gatehouse P, Reese TG, Keegan J, Ferreira PF, Collins S, Speier P, Feiweier T, Silva R. Erratum to In vivo diffusion tensor MRI of the human heart: Reproducibility of breath-hold and navigator based approaches (Magn Reson Med 2013; 70: 454–465). Magn. Reson. Med. 2014;72:599.
49. Jones DK, Basser PJ. “Squashing peanuts and smashing pumpkins”: How noise distorts diffusion-weighted MR data. Magn. Reson. Med. [Internet] 2004;52:979–993.
50. Stanisz GJ, Odrobina EE, Pun J, Escaravage M, Graham SJ, Bronskill MJ, Henkelman RM. T1, T2 relaxation and magnetization transfer in tissue at 3T. Magn. Reson. Med. 2005;54:507–512.
51. Aliotta E, Moulin K, Magrath P, Ennis DB. Quantifying precision in cardiac diffusion tensor imaging with second-order motion-compensated convex optimized diffusion encoding. Magn. Reson. Med. 2018:1–14. doi: 10.1002/mrm.27107.
52. Alam MH, Auger D, McGill L-A, Smith GC, He T, Izgi C, Baksi AJ, Wage R, Drivas P, Firmin DN. Comparison of 3 T and 1.5 T for T2* magnetic resonance of tissue iron. J. Cardiovasc. Magn. Reson. 2016;18:40.
53. Greenspan H, Oz G, Kiryati N, Peled S. MRI inter-slice reconstruction using super-resolution. Magn. Reson. Imaging 2002;20:437–446.
54. Chen W, Sica CT, Meyer CH. Fast conjugate phase image reconstruction based on a Chebyshev approximation to correct for B0 field inhomogeneity and concomitant gradients. Magn. Reson. Med. 2008;60:1104–1111. doi: 10.1002/mrm.21703.
55. Pruessmann KP, Weiger M, Scheidegger MB, Boesiger P. SENSE: sensitivity encoding for fast MRI. Magn. Reson. Med. [Internet] 1999;42:952–962.
56. Lustig M, Donoho DL, Santos JM, Pauly JM. Compressed sensing MRI. IEEE Signal Process. Mag. 2008;25:72–82.
57. Griswold MA, Jakob PM, Heidemann RM, Nittka M, Jellus V, Wang J, Kiefer B, Haase A. Generalized autocalibrating partially parallel acquisitions (GRAPPA). Magn. Reson. Med. 2002;47:1202–1210.